

Design Optimization of the U-Type Oscillating Water Column Wave Energy Converters

Chen-Chou Lin^{1,2*} Duy Tong Nguyen^{1,3} Yi-Chih Chow^{1,3}

¹ Center for Ocean Energy System, College of Engineering, National Taiwan Ocean University, Taiwan

² Department of Mechanical & Mechatronic Engineering, National Taiwan Ocean University, Taiwan

³ Department of Systems Engineering & Naval Architecture, National Taiwan Ocean University, Taiwan

ABSTRACT

Considering the medium wave resources in Taiwan, the oscillating water column (OWC) shows several advantages upon implementation. The installation and maintenance cost of an OWC is relatively lower, and the concrete structure is more survivable under seawater impact and erosion. Survivability is a primary concern because Taiwan suffers from extreme weather during typhoon season, and the OWC structure can withstand harsh conditions. This paper focuses on the design optimization of the U-OWC by establishing a general design procedure to achieve optimal energy capture performance. The optimal geometrical design is critical for implementing Taiwan's OWC wave power system. We establish the optimal chamber design procedure through a two-dimensional numerical simulation and artificial neural network (ANN) approach. Finally, the performance of the optimal design is compared with the design of a previous paper. The result shows that the capture factor of the optimized chamber geometry of U-OWC is 21.9% higher than the previous design.

Keywords: Oscillating Water Column, Optimization, Artificial neural network, Chamber, Capture factor, Response amplitude operator.

* Corresponding author, E-mail: cclin@email.ntou.edu.tw

Received 15 August 2022, Accepted 11 October 2022.

1 INTRODUCTION

Several Oscillating Water Column (OWC) plants integrated with breakwaters have been operated. For example, the wave power plant at Sakata harbor, Japan, which employed a Wells turbine installed in the breakwater (Suzuki et al., 2004), the U-OWC at the harbor of Civitavecchia, Italy (Arena et al., 2013), and Mutriku Wave Power Plant at the port of Mutriku, Spain (Torre-Enciso et al., 2009). Considering the medium level wave resources in Taiwan, the OWC shows some advantages upon implementation. First, the OWCs can be integrated into onshore structures, such as breakwater, mainly a reinforced concrete structure. The installation and maintenance cost of an OWC is relatively lower, and the concrete structure is more survivable under seawater impact and erosion. Survivability is a primary concern because Taiwan suffers from extreme weather during typhoon season, and the OWC structure can withstand harsh conditions. The OWC has been studied comprehensively among various types of Wave Energy Converters (WEC) (Falcão and Henriques, 2016). Since the 1970s, OWCs have been studied in areas of theoretical analysis (Evans et al., 1978; Malmo and Reitan, 1985; Deng et al., 2014), numerical simulation (Hong et al., 2004; Luo et al., 2014; Vyzikas et al., 2017), and experiment (Sarmiento et al., 1992; He et al., 2013; Wang et al., 2018). Chamber geometry is considered the most crucial factor affecting OWC's performance. Rezanejad et al. (2013) analyzed the effect of stepped bottom on the efficiency of the nearshore OWC based on the two-dimensional linear water wave theory. Bouali and Larbi (2013) used ANSYS to investigate the geometry and dimensions of the OWC to obtain the maximum power available in progressive wave characteristics. Kim et al. (2020) applied the potential flow simulation to describe the hydrodynamic response of an inclined OWC. López et al. (2021) used OpenFOAM simulation to compare with experimental results, suggesting the optimized geometry of L-type OWC (L-OWC) and U-type OWC (U-OWC) under the wave conditions at the Port of Vigo, Spain. The results showed that the L-OWC has better performance than the U-OWC. The L-OWC geometry has a shallow entrance, a high horizontal chamber duct, and a vertical duct, delivering the maximum capture-width ratio of 71.6%. Tsai et al. (2018) investigated the Performance of a Modified Breakwater-Integrated OWC WEC under Taiwan's wave climate using Flow-3D simulation and the experimental investigation. Their numerical simulation in full-scale showed that the hydrodynamic efficiency could reach 83% when the air orifice area ratio is 0.7%. Regarding geometric optimization, methodologies based on machine learning or neural network have emerged in recent years. For example, Lin et al. (2019) established an artificial neural network (ANN) model to study the performance of cylindrical oscillating wave surge converters (OWSCs) and obtained a geometric shape with a very high value of capture factor (CF); Liu et al. (2020) applied ANN to predict the CFs of OWSCs and a genetic algorithm to search for the optimal result. The L-OWC and U-OWC have their pros and cons. With respect to the performance, the L-OWC generally has much higher energy conversion efficiency, i.e., higher CF or capture width ratio (CWR), compared with the U-OWC, while the U-OWC has a broadband performance, i.e., its CF is more uniformly behaved among the wave spectrum. With respect to the cost, the L-OWC is usually bulkier in size than the U-OWC, meaning that the material and installation cost of the L-OWC will be more expensive. It depends on developers to decide which model is the "best" selection after careful calculations and considerations. In this paper, we shall focus on the U-OWC due to its broadband behavior. Optimal geometric design is critical for implementing Taiwan's OWC wave power system. This paper establishes the optimal chamber design procedure through two-dimensional numerical simulation and the ANN approach. The optimal design will be compared with the previous design by López et al. (2021).



2 DESIGN AND ANALYSIS METHODOLOGY

2.1 OWC Design Theory

The theoretical methodology used in the present paper was adapted from Chow et al. (2018) and Chow et al. (2022). The free surface of the water column in the OWC's chamber was assumed to be a massless, piston-like oscillator moving up (+y) and down (-y) with $y = 0$ as the still-water level (SWL). A plane wave is incident with amplitude A_i and angular ω , making the free surface oscillate harmonically with ω as $Y(t)$, i.e.,

$$Y(t) = \text{Re}[A_Y e^{-i\omega t}] \quad (1)$$

where A_Y denotes the complex amplitude of $Y(t)$. The equation of the harmonic motion for the OWC can be written as

$$\begin{cases} F_E = (-\omega^2 \mu_A - i\omega v_R + \rho g S + Z_{PTO+C}) A_Y \\ Z_{PTO+C} = \left(\frac{\omega^2 v_{PTO}^2}{\omega^2 v_{PTO}^2 + C_{air}^2} \right) C_{air} - i\omega \left(\frac{C_{air}^2}{\omega^2 v_{PTO}^2 + C_{air}^2} \right) v_{PTO} \end{cases} \quad (2)$$

where F_E denotes the complex amplitude of the wave exciting force; μ_A the added mass due to the oscillation of the water column; v_{PTO} and v_R the damping coefficients due to the PTO (Power Take-off) and the wave radiation effect, respectively; C_{air} the spring-like coefficient due to the effect of the air compressibility incurred in the OWC; ρ the density of the sea water; g the acceleration of gravity; S the area of the free surface of the water column in the OWC's chamber. After some algebraic operations, Eq. (2) can be transformed into

$$|A_Y|^2 = \frac{|F_E|^2}{\mu_A^2 (\omega^2 - \omega_o^2)^2 + \omega^2 (v_R + v'_{PTO})^2} \quad (3)$$

where

$$\begin{cases} \omega_o = \sqrt{\frac{C'_{air} + \rho g S}{\mu_A}} \\ C'_{air} = \left(\frac{\omega^2 v_{PTO}^2}{\omega^2 v_{PTO}^2 + C_{air}^2} \right) C_{air} \\ v'_{PTO} = \left(\frac{C_{air}^2}{\omega^2 v_{PTO}^2 + C_{air}^2} \right) v_{PTO} \end{cases} \quad (4)$$

The term ω_o , similar to a natural frequency, can be regarded as a characteristic frequency of the OWC due to the effective coefficient of air compressibility C'_{air} . The coefficient v'_{PTO} can be regarded as the effective damping coefficients due to the PTO. The average power in a wave period T ($T = 2\pi/\omega$) that is transmitted to the PTO can be calculated using

$$P = \frac{1}{T} \int_0^T v_{PTO} \left(\mathbf{Y}_{PTO} \right)^2 dt = \frac{\omega^2 v'_{PTO}}{2} |A_Y|^2 \quad (5)$$

Finally, the capture factor CF can be expressed as

$$CF = \frac{P}{P_i} = \frac{P}{\frac{1}{2} \rho g |A_i|^2 C_g B} = \left(\frac{\omega^2 v'_{PTO}}{\rho g |A_i|^2 C_g B} \right) |A_Y|^2 \quad (6)$$

where P_i denotes the incident wave power received within the OWC's width B ; C_g the group velocity of the incident wave.

Combining Eqs. (3) and (6) and performing some algebra, CF can be expressed as

$$CF = \left(\frac{|F_E|^2}{2 \rho g |A_i|^2 v_R C_g B} \right) \left[\frac{2(v_R \cdot v'_{PTO})}{\omega^2 \mu_A^2 \left(1 - \left(\frac{\omega_o}{\omega} \right)^2 \right)^2 + (v_R + v'_{PTO})^2} \right] \quad (7)$$

It can be shown that when

$$\begin{cases} \omega_o = \sqrt{\frac{C'_{air} + \rho g S}{\mu_A}} = \omega \\ v'_{PTO} = v_R \end{cases} \quad (8)$$

the OWC reaches its resonance and the CF becomes the maximum as

$$CF_{@res} = \frac{|F_E|^2}{4 \rho g |A_i|^2 v_R C_g B} \quad (9)$$

From Eq. (9), it is evident that CF increases with a decreasing v_R , leading to an obvious design guideline for reducing the wave radiation from the OWC as much as possible. For example, the U-type OWC has its water entrance opening close to the sea surface; the farther the opening to the sea surface, the less easily the energy radiates out of the OWC, i.e., the smaller the v_R .

Assuming that the air in the OWC's chamber is undergoing an isentropic process of compression and expansion respectively due to the rise and fall of the water column, the compressibility coefficient C_{air} can be modeled as

$$C_{air} = \frac{k_{air} p_{atm} S}{h_{chamber}} \quad (10)$$

where $k_{air} = 1.4$ is the specific-heat ratio of the air; $h_{chamber}$ the distance between the water surface at the SWL in the chamber and the top wall of the chamber; p_{atm} the atmospheric pressure. Combining the first line of Eq. (8) and Eq. (10), and reasonably assuming $C_{air} \approx \omega v_{PTO}$ and substituting it into Eq. (4), one can obtain



$$\begin{cases} C'_{air} \approx \left(\frac{\omega^2 v_{PTO}^2}{2\omega^2 v_{PTO}^2} \right) C_{air} = \frac{C_{air}}{2} \\ \omega_o \approx \sqrt{\frac{C_{air}/2 + \rho g S}{\mu_A}} = \sqrt{\frac{(k_{air} p_{atm} + 2\rho g h_{chamber}) S}{2h_{chamber} \mu_A}} = \omega \end{cases} \quad (11)$$

In order to satisfy Eq. (11), one needs to design a set of geometric parameters including S , $h_{chamber}$, and μ_A to form the characteristic frequency ω_o to match the principal incident wave frequency ω . In view of the goal of developing a broad-band-responsive OWC, the second fraction's denominator in Eq. (7) suggests that the lesser the μ_A , the broader the band of the OWC.

This OWC theory can serve as a useful design guideline because it integrates all mechanism components critical to the OWC's performance and elucidates the relations among them, e.g., C'_{air} and v'_{PTO} are related with both C_{air} and v_{PTO} . It can also be used as a tool for the regression and curve fitting of the data obtained from OWC experiments or numerical simulations to estimate those important hydrodynamic coefficients associated with a specific OWC geometry, e.g., $|F_E|$, v_R and μ_A . This estimation sheds new light on how to achieve both high-peak power output and broad-band-responsive performance in the design. However, it requires a large amount of data and is obviously beyond the scope of the present paper. Therefore, we will leave this interesting work which combines theory and numerical simulation to future studies.

2.2 The Design Procedure

The OWC design procedure mainly includes two steps: 1. Verification of simulation software reliability. 2. Optimal geometric design of the OWC chamber. This study applies the commercial software Flow-3D to simulate the hydrodynamic behavior of the U-type OWC and design the chamber geometry of the OWC; the software's reliability must be confirmed first. Step 1 is carried out through OWC model wave tank tests. The data of the model tests is used to validate the results of the numerical simulation. In step (2), the U-type OWC performance database of selected conditions, including different chamber dimensions and wave conditions, is established. The optimal geometry of the chamber can be found through the artificial neural network training and prediction process.

2.3 Experimental Validation

In order to validate the simulation results, a 1/20th scale model experiment was conducted. The experiments were performed in a wave tank of the Hydraulic Laboratory located at the Department of Harbor & River Engineering of National Taiwan Ocean University. Figure 1 shows the layout of the experimental setup for this model experiment. We used a high-speed camera to capture water level images in time series inside the OWC chamber and developed an image processing and analysis procedure to yield the positions of moving water levels.

2.3.1 Wave tank and incident wave conditions

The wave tank used in the experiment is 28 m long, 2.0 m wide, and 0.8 m high. As shown in Figure 2, the wavemaker, designed and manufactured by Edinburgh Design Ltd., can generate regular and irregular waves according to user's instructions. Wave gauges were set at the longitudinal middle plane of the wave tank.

There are four incident wave conditions: the combinations of two wave periods of 1.9 sec and 2.35 sec and two wave heights of 0.05 m and 0.075 m, which are adopted and scaled-down (1/20th) from the wave data of

coastal waters of northeast Taiwan, as shown in Table 1. The water depth in the wave flume in the experiment was kept at 0.5 m.

Table 1. Incident wave conditions of numerical simulation and experiments.

Parameters	scaled dimension (1/20 th)
Wave height H	0.05 m, 0.075 m
Wave period T	1.9 s, 2.35 s
Water depth h	0.5 m
Wave number kh	0.679, 0.823

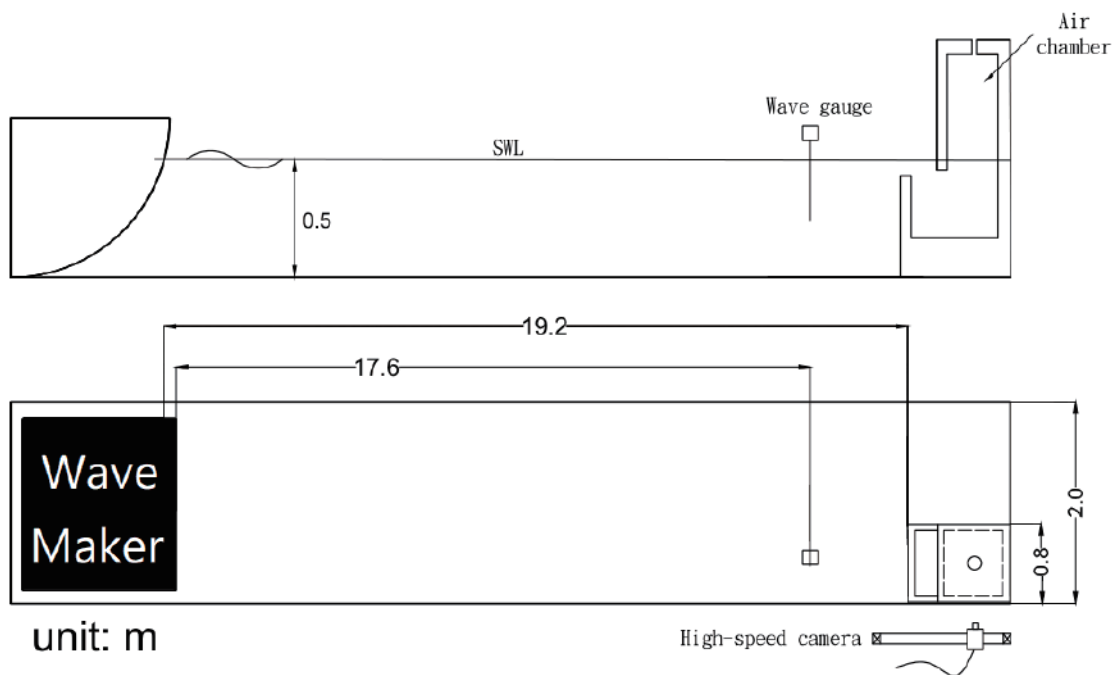


Figure 1. Schematic of the OWC model experimental setup.



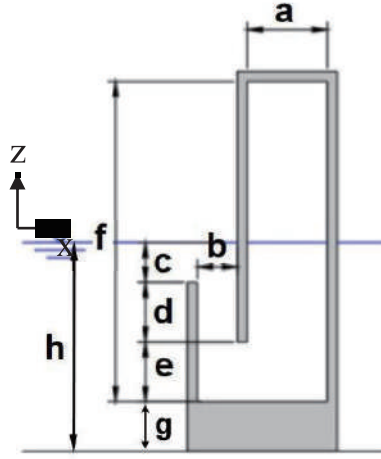
Figure 2. Displacement piston wavemaker and the wave tank.

2.3.2 The experimental model specifications

As mentioned above, experiments were conducted to verify the accuracy of the numerical results. Therefore, all the parameters of the U-OWC experimental model correspond to its numerical setup. Table 2 shows details of the 1/20th scale U-OWC experimental model parameters with two different air chamber slot widths, $w = 0.005$ m and 0.01 m, representing different PTO damping. The above four sets of wave conditions combined with two air chamber slot widths make eight sets of experimental conditions in total. The width of the OWC model in the transverse direction of the wave tank was chosen to be 0.8 m (Figure 1) so that the model can maintain not only its structural strength and rigidity, but also quasi-2D flow features of the water in the conduit and air chamber verified with the observations of the almost flat and horizontal free surface during the oscillations of the water column.

Table 2. Geometric parameters of 1/20th scaled baseline model of U-OWC.

Model Parameter	Size (m)
Chamber width a (X-dir)	0.198
Front channel width b	0.1
Depth of front channel c	0.1
Height of front wall $d+e$	0.3
Height of chamber inlet e	0.15
Height of chamber f	0.805
Height of foundation g	0.1
Water depth h	0.5
Chamber width B (Y-dir)	0.3
Slot (orifice) width w	0.005, 0.01



2.3.3 Numerical simulation

Figure 3 shows the computational domain and mesh settings with the U-OWC model inside. The meshing with two blocks is adopted; one is the wave area block (block 1), the other is the flap-motion block (block 2). Details of the mesh setting are shown in Table 3. The RANS simulations are carried out using the software package FLOW-3D to conduct this two-fluids modeling problem, and the $k-\omega$ model is chosen. Fluid 1 is water at 20 degrees and fluid 2 is air at 25 degrees. The small-scale model simulation can ignore air compressibility (Elhanafi et al., 2017). Therefore, both water and air are treated as incompressible flow in this series of simulations.

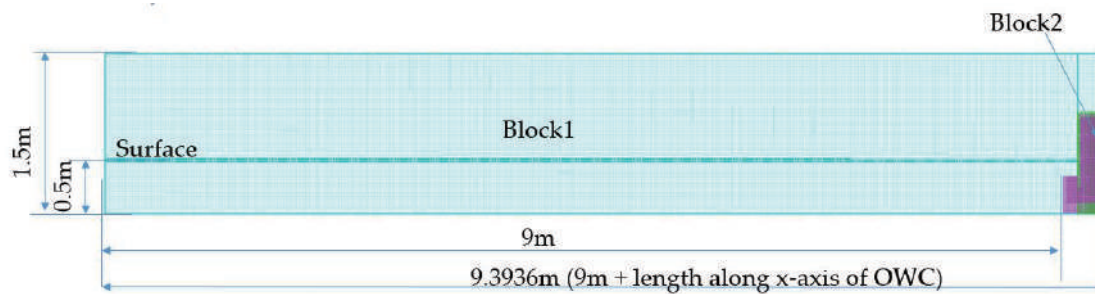

Figure 3. The schematic of the computation domain and mesh setting.


Table 3. The mesh setting of the computation domain (unit in m).

	X	Y	Z
Block 1 (wave domain)	$X_{\min} = 0$	$Y_{\min} = 0$	$Z_{\min} = -0.5$
	$X_{\max} = 9.3936$	$Y_{\max} = 0.008$	$Z_{\max} = 1$
	$\Delta x = 0.02$	$\Delta y = 0.008$	$\Delta z = 0.02$
Block 2 (OWC)	$X_{\min} = 9$	$Y_{\min} = 0$	$Z_{\min} = -0.5$
	$X_{\max} = 9.3936$	$Y_{\max} = 0.008$	$Z_{\max} = 0.5$
	$\Delta x = 0.04$	$\Delta y = 0.004$	$\Delta z = 0.04$

The Response Amplitude Operator (RAO) is used to evaluate the response of the different OWC designs under different incident wave conditions, according to López et al. (2021). The RAOs includes RAO_c and RAO_p , where RAO_c represents the response amplitude operator of the water level difference inside the chamber, and RAO_p represents the response amplitude operator of pressure difference.

The definitions are expressed as follows

$$RAO_c = \frac{H_c}{H_i} \quad (12)$$

$$RAO_p = \frac{\Delta p}{\rho_w g H_i} \quad (13)$$

where H_i is the incident wave height, H_c is the average water level difference of the water column inside the chamber, Δp is the air pressure difference, ρ_w is the density of water, and g is the acceleration of gravity.

Since the measurement of the air pressure difference requires fairly accurate measuring instruments, this paper will only use RAO_c to compare results between numerical simulation and the experiment.

The capture factor CF , which is the ratio between captured power and incident wave power, can be rewritten as equation (14):

$$CF = \frac{P_{air}}{P_i} = \frac{P_{air}}{\frac{1}{8} B \rho_w g H_i^2 C_g} \quad (14)$$

$$P_{air} = \frac{1}{T} \int_0^T P_E dt = \frac{1}{T} \int_0^T \Delta p \cdot Q dt \quad (15)$$

$$P_E = \Delta p \cdot Q \quad (16)$$

Among which, P_{air} represents the average power of air to PTO (such as turbine), P_E is the instantaneous power of the air, and P_i is the incident wave power per unit.

2.3.4 High-speed imaging

As shown in Figure 4, the Phantom v310 CMOS high-speed camera with a maximum resolution of 1280 x 800 pixels and an acquisition rate as high as 3200 fps was used to capture the water level inside the U-OWC chamber model (shown in Figure 5) through the transparent tempered glass on the sidewall of the wave flume.

The wave gauges and the high-speed camera were installed together to simultaneously capture the time series of the change of incident wave height and the water level inside the OWC chamber.



Figure 4. Phantom v310 CMOS high-speed camera.



Figure 5. The water level line inside the U-OWC chamber.



2.3.5 Image processing and analysis procedures

The image processing and analysis procedures are shown in Figure 6. The original image of the time series of the water-air interface inside the OWC chamber is loaded into the MATLAB program for image processing, including denoising, contrast enhancement, filtering, etc.

The water level can be clearly distinguished after using Canny edge detection. Then, it is easy to position each point on the water level line, and the positions of all points on the water level line are averaged to obtain the average position of the water level line. Finally, we can then calculate the average distance between the upper and lower bounds of the water level, H_c in equation (12).

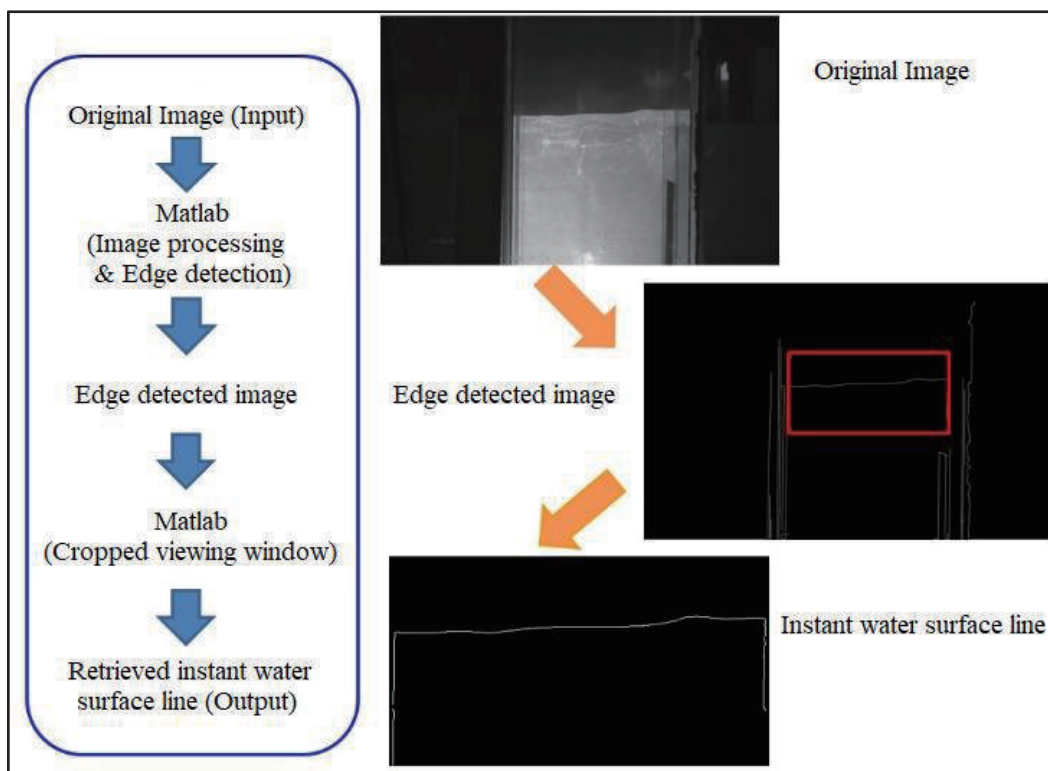


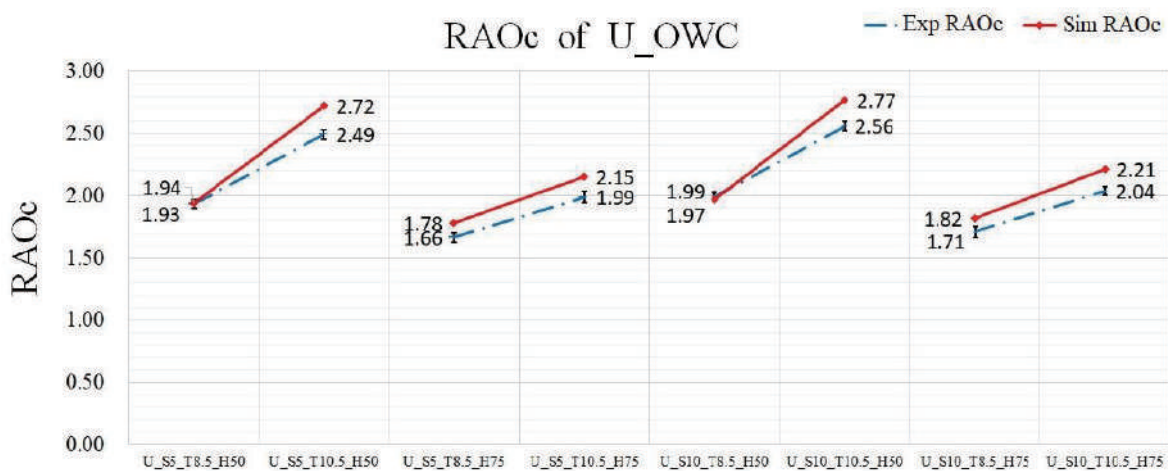
Figure 6. The image processing and analysis procedures.

2.3.6 Comparison between experimental and numerical simulation results

Figure 7 and Table 4 compare the experimental and numerical simulation results of U-OWC. The value of each experiment is the average value recorded after three repetitions. First, it is clear that the RAO_c values of numerical simulations are larger than those of the experiments primarily. The differences are around 6% – 9%, among which the minimum difference compared with the experiment is 0.35%. These differences may be caused by some phenomena that cannot be observed in the experiment, including friction loss on the wall surface. When the response amplitude is large, the water surface inside the air chamber will be drawn into the air near the channel, thus causing errors. Overall, the experimental results are reasonable compared with numerical results in terms of the average difference values. Therefore, the reliability of this U-OWC's numerical simulation using the current software should be considered acceptable.

Table 4. RAO_c of experimental and numerical simulation.

Slot width w Wave conditions (T, H)	RAO_c Experimental	RAO_c Simulated	Difference %
$w=0.005\text{m} / T=1.9\text{s} / H=0.05\text{m}$	1.93	1.94	0.35
$w=0.005\text{m} / T=2.35\text{s} / H=0.05\text{m}$	1.66	1.78	7.05
$w=0.005\text{m} / T=1.9\text{s} / H=0.075\text{m}$	2.49	2.72	9.18
$w=0.005\text{m} / T=2.35\text{s} / H=0.075\text{m}$	1.99	2.15	8.12
$w=0.01\text{m} / T=1.9\text{s} / H=0.05\text{m}$	1.99	1.97	-1.19
$w=0.01\text{m} / T=2.35\text{s} / H=0.05\text{m}$	1.71	1.82	6.54
$w=0.01\text{m} / T=1.9\text{s} / H=0.075\text{m}$	2.56	2.77	8.26
$w=0.01\text{m} / T=2.35\text{s} / H=0.075\text{m}$	2.04	2.21	8.48


 Figure 7. Comparison of RAO_c of U-OWC experimental and simulation results.

2.4 Optimization of OWC Chamber

There is a highly nonlinear functional relationship between the input (model's geometric parameter) and output (capture factor). In the artificial neural network, the above functional relationship is represented by the input data (Input) and the target value (Target). The fitting tool in Matlab can, based on the artificial neural network algorithm, find this functional relationship when given a set of input-output data. These data sets will be used to train the network and search for the best functional relationship.

The artificial neural network fitting tool (Nftool) in Matlab mainly uses three algorithms: 1. Bayesian Regulation (BR), 2. Levenberg Marquardt (LM) and 3. Scaled Conjugate Gradient (SCG) to train the static fitting of a standard two-layer feedforward neural network. Generally, the Bayesian Regulation algorithm can obtain relatively good prediction results when dealing with a small number of samples but relatively more noise. The number of training data here is about 200, so we used the Bayesian Regulation algorithm.



Training data is established from the results of numerical simulation. Various sets of design parameters of OWC's chamber are fed into the Flow-3D to obtain the results, i.e., the corresponding capture factor. The data sets are randomly divided into 70% for training, 5% for validation, and 25% for testing. The ANN performance is evaluated using mean square error (MSE) and regression analysis. The training data set is used to adjust the ANN's weights according to the error. The test data set provides a way to analyze ANN performance during and after training, so the test data does not affect training. When the generalization process stops improving (note: generalization is the ability of a machine-learning algorithm to adapt to fresh samples), training stops automatically.

The more training data provided, the higher the prediction accuracy. Therefore, we must first provide a sufficient amount of data to improve the prediction accuracy of the ANN. In Table 2, we have selected five parameters, which are the width of the air chamber a , the width of the front channel opening b , the depth of the front channel c , the height of chamber inlet e , and the slot width w . We set lower and upper bounds of the five parameters. To establish the training data set, we chose two points in the corresponding range of each design parameter as shown in Table 5. There are three wave periods (1.45s, 1.9s, 2.24s) and two wave heights (0.05m, 0.075m). So in total, there are $2 \times 2 \times 2 \times 2 \times 2 \times 3 \times 2 = 192$ combinations of parameters for the simulation of the U-OWC.

We adopted Bayesian Regulation algorithm for the training process. The ANN is implemented by one hidden layer with ten cells. Figure 8 shows the results of the training. The performance is considered to be a good fit where Training R is 0.98367, and Test R is 0.92135.

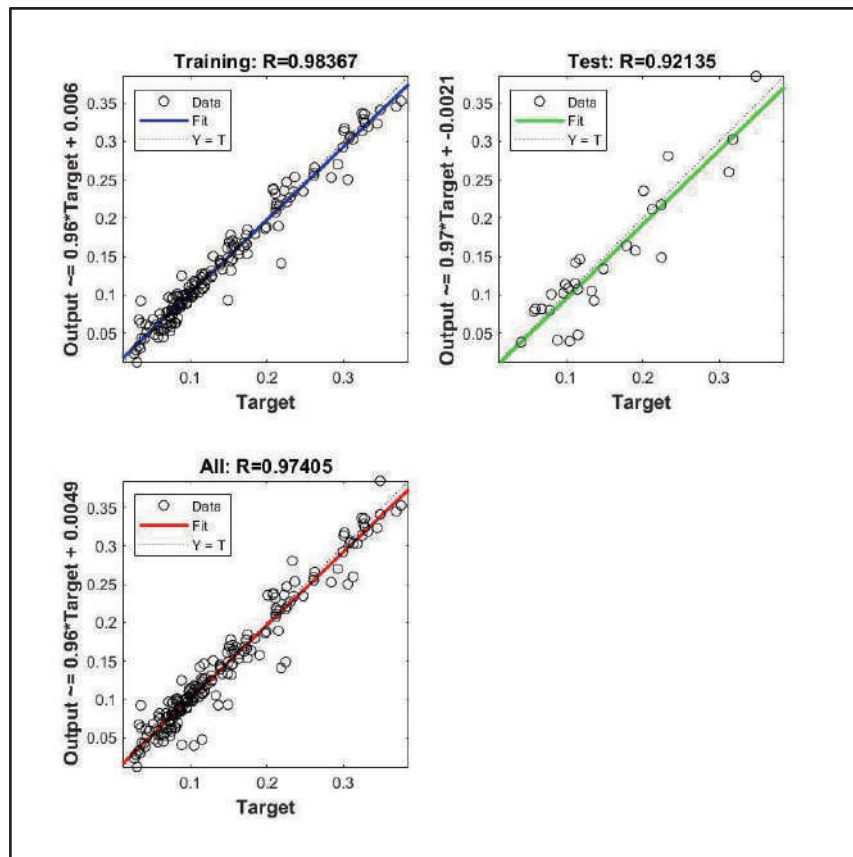


Figure 8. Training performance of the ANN for U-OWC.

Table 5. The lower bounds, upper bounds, increments, and number of sampled points for ANN training and prediction (unit in m).

Design parameter	Lower bound	Upper bound	Lower/Upper points of training data	Increment of sampled points for prediction	Number of sampled points for prediction
a	0.17	0.29	0.2/0.3	0.002	61
b	0.095	0.155	0.1/0.15	0.005	13
c	0.095	0.155	0.1/0.15	0.005	13
e	0.14	0.235	0.15/0.225	0.005	20
w/a	0.01333	0.03	0.01333/0.03	0.00333	6

After the ANN training/learning is completed, the ANN can predict the capture factor of any sampled points with all combinations of a , b , c , e , and w/a inside the range of each design parameter. The performance prediction for U-OWC focuses on a wave period of 1.9 seconds (corresponding to $T = 8.5$ s and $H = 1.5$ m in real sea). The parameter sets of sampled points for prediction within the designated range of each parameter is specified in Table 5. The total number of the parameter sets for prediction is $61 \times 13 \times 13 \times 20 \times 6 = 1,237,080$. Finally, the maximum CF value can be found from all predicted CF s. It took about 25 seconds to complete all the CF predictions and search for the maximum CF value. The optimal design parameters were then fed back into Flow-3D to get the simulation result for comparison. Table 6 shows the final result of the ANN optimization for the U-OWC chamber, where CF_{ANN} denotes the predicted maximum CF value by ANN, and CF_{F3D} denotes the CF obtained from Flow-3D's simulation with the same design parameters. The result shows that the CF_{F3D} obtained by Flow-3D simulation is smaller than the CF_{ANN} obtained by ANN's prediction, and the simulated value is about 80.5% of the predicted value of ANN. We must emphasize that the ANN's predicted value, CF_{ANN} , is based on the regression analysis of the input data set (called the training process). If the input training data cannot fully characterize the whole range, discrepancies will occur at certain regions. In the current case, as shown in the training window of Figure 8, most data are distributed below the output value of 0.15, while the training data above the output value of 0.3 are relatively sparse. This will result in discrepancies between CF s of ANN-predicted and numerical simulation, specifically in the higher CF region ($CF > 0.3$).

Table 6. The optimization result of U-OWC ($T = 1.9$ s).

Design parameter	Optimal design value (m)	CF_{ANN}	CF_{F3D}
Chamber width a	0.17	0.539	0.434
Front channel width b	0.155		
Depth of front channel c	0.155		
Height of chamber inlet e	0.14		
Slot width ratio w/a	0.01333		



Although the predicted CF_{ANN} value is over-estimated, the corresponding design parameter values that make the CF become local maximum are more important. In this paper, we prove that the simulated result CF_{F3D} is a local maximum with the same design parameter values of the maximum CF_{ANN} .

To prove that the $CF_{F3D} = 0.434$ is a local maximum, we performed the simulation of the U-OWC with a design value $\pm 5\%$ from the current optimal design parameters using the FLOW-3D. Here we fixed the slot width ratio w/a ($= 0.01333$) since the smaller the w/a value the larger the CF that can be guaranteed due to a larger damping effect. Hence 8 neighboring points with a $\pm 5\%$ variation from the optimal design parameter values are simulated. The results are as in Table 7, which shows that all points neighboring the optimal design point have smaller CF values than the maximum CF_{F3D} (0.434). Hence the optimal design parameters obtained by the ANN can also achieve maximum simulated CF_{F3D} .

Table 7. The CF values of points neighboring the optimal design point. (Max. CF_{F3D})

Design parameter	Optimal design value (Odv) (m)	CF of neighboring points		Max. CF_{F3D}
		Odv-5%	Odv+5%	
Chamber width a	0.17	0.401	0.385	0.434
Front channel width b	0.155	0.411	0.371	
Depth of front channel c	0.155	0.410	0.424	
Height of chamber inlet e	0.14	0.378	0.345	
Slot width ratio w/a	0.01333			

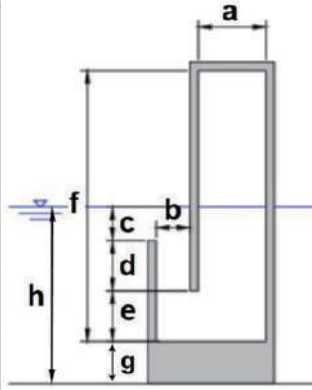
3 RESULTS AND DISCUSSION

3.1 Optimization Results

After the optimization design process, the 1/20th model scale U-OWC shown in Table 8 was obtained; the size specifications of López et al. (2021) are presented for reference. The result was based on the wave period $T = 1.9$ sec (corresponding to 8.5 sec in real sea), the wave height $H = 0.075$ m (corresponding 1.5 m in real sea), and the water depth $h = 0.5$ (corresponding to 10 m in real sea).

Table 8. Optimal chamber design parameters and López's spec. of U-OWC.

Design parameters of chamber	Size (m)	
	López et al. (2021)	Present optimal design
Chamber width a	0.16	0.17
Front channel width b	0.08	0.155
Depth of front channel c	0.08	0.155
Height of chamber inlet e	0.12	0.140
Slot (orifice) width ratio w/a	0.0121	0.0133



3.2 Performance Evaluation of Optimal Chamber Design

Figure 3-2 shows the capture factor (CF) of U-OWC when optimizing the design parameters using the ANN based optimization scheme. It can be found that the power capturing efficiency is the highest when the wave period is 6.5 seconds, where the CF is 0.463. At an 8.5-second wave period, the CF dropped slightly to 0.434, and at a 10-second wave period, the CF dropped to 0.365. Then, the CF dropped drastically to 0.205 at an 11-second wave period, and 0.16 at a 12-second wave period. The above results suggest that the optimal design in this study perform better at shorter wave periods than longer wave periods. By comparing with previous literature (López et al., 2021), it is found that the U-OWC has the best capture efficiency CF at 8 seconds. The optimized results in this study show that the CF (0.434 at 8.5 seconds) in this study is 21.9% higher than the best CF (0.356 at 8 seconds) in the previous paper. As shown in Figure 3-2, the CF drops by approximately 21% between periods of 6.5 seconds and 10 seconds. Regarding the wave conditions of Taiwan's northeastern water and Taichung Port, the wave period between 6 seconds and 10 seconds behaves with larger wave energy potential. Therefore, the optimized chamber design can be applied in the Taiwanese waters just mentioned. The other advantage of the current design is that the power capturing performance is relatively stable in the period range between 6 and 10 seconds.

Figures 10(a) and 10(b) show the RAO_c and RAO_p of the optimized U-OWC, respectively. RAO_c exhibits a monotonically increasing trend with the period, while the rate of increase gradually decreases with the period. RAO_p peaks around 8.5 seconds and exhibits stable performance with respect to wave period (frequency).

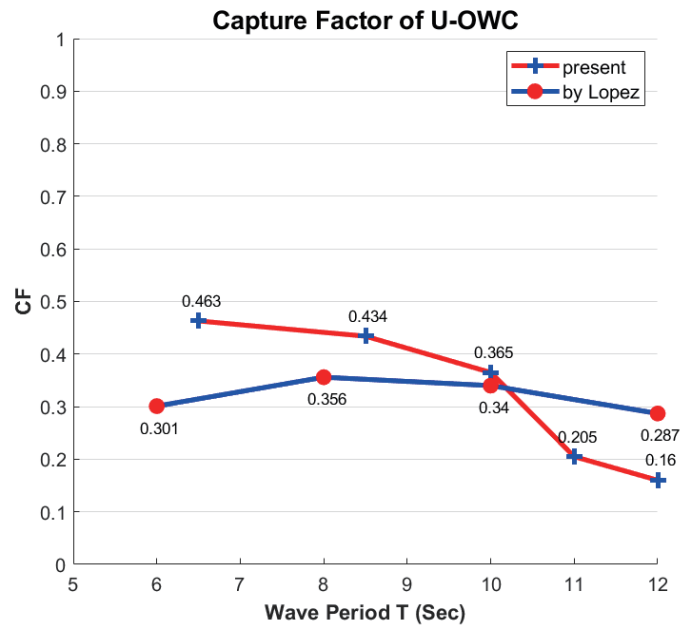


Figure 9. The capture factor of the optimized U-OWC (in red line) and López's (in blue line).

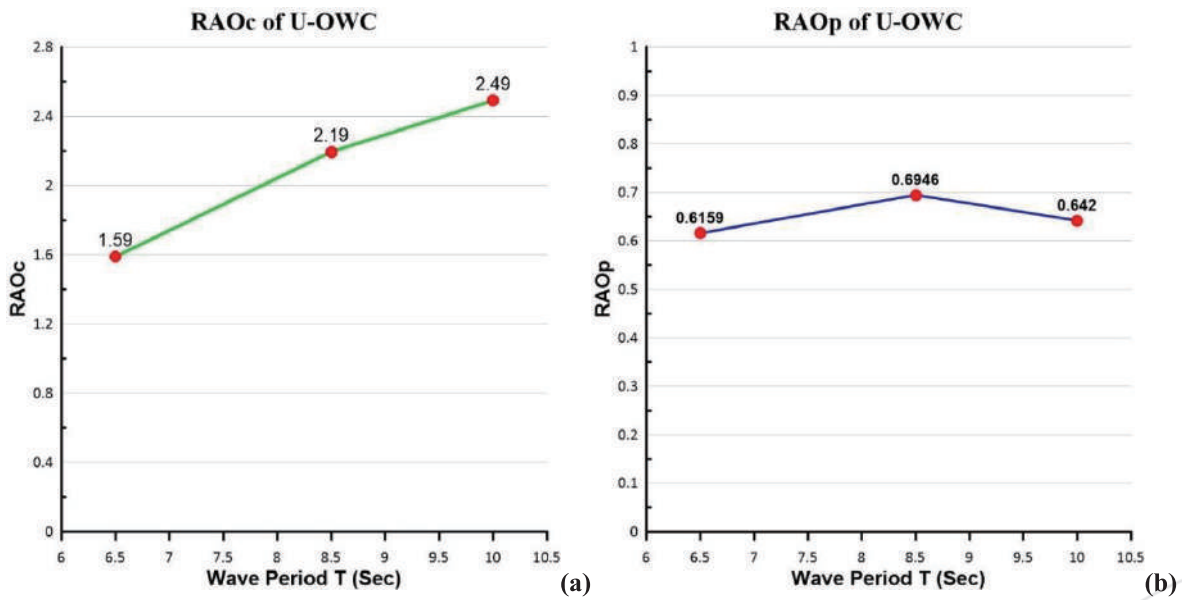


Figure 10. Performance of U-OWC optimized design (a) RAO_c (b) RAO_p .

4 CONCLUSIONS

The paper demonstrates the optimization process for the chamber design of U-type OWC wave energy converters. We employed the ANN algorithm to obtain the functional relationship between the input design parameters and the capture factor, and the ANN can predict the capture factor efficiently. The final optimized chamber design shows better performance in power capturing efficiency than the design of the previous paper. Conclusions are as follows.

1. The geometry of the U-OWC's chamber significantly affects its power capture performance. The optimal design of the U-OWC in this research has a *CF* of 0.434 at 8.5-s wave periods, which is 21.9% higher than the *CF* under the same wave condition of the best design in the previous paper (López et al., 2021).
2. The current optimal design has a better performance in the short-period region (6.5 s – 10 s), which fits the wave climate pattern in Taiwan's waters.
3. The design optimization based on the ANN approach has high efficiency in performance prediction, even though the predicted values are higher than the simulated values. The prediction accuracy can be improved by providing an input database with a uniformly-distributed dataset.

ACKNOWLEDGEMENTS

The authors would like to thank National Academy of Marine Research for providing financial support, technical expertise, and guidance.

REFERENCES

- Arena, F., Romolo, A., Malara, G., & Ascanelli, A. (2013). On design and building of a UOWC wave energy converter in the Mediterranean Sea: A Case Study. *ASME 2013 32nd International Conference on Ocean, Offshore and Arctic Engineering*, 8. <https://doi.org/10.1115/OMAE2013-11593>
- Bouali, B. & Larbi, S. (2013). Contribution to the Geometry Optimization of an Oscillating Water Column Wave Energy Converter. *Energy Procedia*, 36: 565-573. <https://doi.org/10.1016/j.egypro.2013.07.065>
- Chow, Y. C., Chang, Y. C., Chen, D. W., Lin, C. C., & Tzang, S. Y. (2018). Parametric design methodology for maximizing energy capture of a bottom-hinged flap-type WEC with medium wave resources. *Renewable Energy*, 126: 605-616. <https://doi.org/10.1016/j.renene.2018.03.059>
- Chow, Y. C., Jhang, J. K., Nguyen, D. T., & Lin, C. C. (2022). A Novel Design and Optimization Methodology of Oscillating Water Column Wave Energy Converters. *Proceedings of the Renewable Energy*.



- Deng, Z., Huang, Z., & Law, A. W. K. (2014). Wave power extraction from a bottom-mounted oscillating water column converter with a V-shaped channel. *Proceedings of The Royal Society A Mathematical Physical and Engineering Sciences*, 470(2167). <https://doi.org/10.1098/rspa.2014.0074>
- Elhanafi, A., Macfarlane, G., Fleming, A., & Leong, Z. (2017). Scaling and air compressibility effects on a three-dimensional offshore stationary OWC wave energy converter. *Applied Energy* 189: 1-20. <https://doi.org/10.1016/j.apenergy.2016.11.095>
- Evans, D. V. (1978). The Oscillating Water Column Wave-energy Device. *IMA Journal of Applied Mathematics*, 22(4): 423-433. <https://doi.org/10.1093/imamat/22.4.423>
- Falcão, A. F. O. & Henriques, J. C. C. (2016). Oscillating-water-column wave energy converters and air turbines: A review. *Renewable Energy* 85: 1391-1424. <https://doi.org/10.1016/j.renene.2015.07.086>
- He, F., Huang, Z., & Law, W. K. A. (2013). An experimental study of a floating breakwater with asymmetric pneumatic chambers for wave energy extraction. *Applied Energy*, 106: 222-231. <https://doi.org/10.1016/j.apenergy.2013.01.013>
- Hong, D. C., Hong, S. Y., & Hong, S. W. (2004). Numerical study on the reverse drift force of floating BBDB wave energy absorbers. *Ocean Engineering*, 31(10): 1257-1294. <https://doi.org/10.1016/j.oceaneng.2003.12.007>
- Kim, J. S., Nam, B. W., Kim, K. H., Park S., Shin, S. H., & Hong K. (2020). A Numerical Study on Hydrodynamic Performance of an Inclined OWC Wave Energy Converter with Nonlinear Turbine-Chamber Interaction based on 3D Potential Flow. *Journal of Marine Science and Engineering*, 8(3): 176. <https://doi.org/10.3390/jmse8030176>
- Lin, C. C., Chow, Y. C., & Huang, Y. Y. (2019, July 14- July 17). Geometric Optimization of Cylindrical Flaps of Oscillating using Artificial Oscillating Wave Surge Converters Using Artificial Neural Network Models. [ES2019-3878]. Proceedings of the ASME 2019 13th International Conference on Energy Sustainability, Bellevue, Washington, USA.
- Liu, Z., Wabg, Y., & Hua, X. (2020). Prediction and optimization of oscillating wave surge converter using machine learning techniques. *Energy Conversion and Management*, 210: 112677. <https://doi.org/10.1016/j.enconman.2020.112677>
- López, I., Carballo, R., Fouz, D. M., & Iglesias, G. (2021). Design Selection and Geometry in OWC Wave Energy Converters for Performance. *Energies*, 14(6): 1707. <https://doi.org/10.3390/en14061707>
- Luo, Y., Nader, J. R., Cooper, P., & Zhu, S. P. (2014). Nonlinear 2D analysis of the efficiency of fixed Oscillating Water Column wave energy converters. *Renewable Energy*, 64: 255-265. <https://doi.org/10.1016/j.renene.2013.11.007>

- Malmo, O., & Reitan, A. (1985). Wave-power absorption by an oscillating water column in a channel. *Journal of Fluid Mechanics*, 158: 153-175. <https://doi.org/10.1017/S0022112085002592>
- Rezanejad, K., Bhattacharjee, J., & Soares, C. G. (2013). Stepped sea bottom effects on the efficiency of nearshore oscillating water column device. *Ocean Engineering*, 70: 25-38. <https://doi.org/10.1016/j.oceaneng.2013.05.029>
- Sarmiento, A. J. N. A. (1992). Wave flume experiments on two-dimensional oscillating water column wave energy devices. *Experiments in Fluids*, 12: 286-292. <https://doi.org/10.1007/BF00187307>
- Suzuki, M., Arakawa, C., & Takahashi, S. (2004, May 23- May 28). Performance of wave power generating system installed in breakwater at Sakata port in Japan [202-209/ ISOPE-I-04-137]. Proceedings of the 14th International Offshore Polar Engineering Conference, Toulon, France.
- Torre-Enciso, Y., Ortubia, I., De Aguilera, L., & Marqués, J. (2009, September 7- September 10). Mutriku wave power plant: From the thinking out to the reality [Conference presentation]. Proceedings of the 8th European Wave Tidal Energy Conference, Uppsala, Sweden.
- Tsai, C. P., Ko, C. H., & Chen, Y. C. (2018). Investigation on Performance of a Modified Breakwater-Integrated OWC Wave Energy Converter. *Sustainability*, 10(3): 643. <https://doi.org/10.3390/su10030643>
- Vyzikas, T., Deshoulières, S., Giroux, O., Barton, M., & Greaves, D. (2017). Numerical study of fixed Oscillating Water Column with RANS-type two-phase CFD model. *Renewable Energy*, 102(B): 294-305. <https://doi.org/10.1016/j.renene.2016.10.044>
- Wang, R. Q., Ning, D. Z., Zhang, C. W., Zou, Q. P., & Liu, Z. (2018). Nonlinear and viscous effects on the hydrodynamic performance of a fixed OWC wave energy converter. *Coastal Engineering*, 131: 42-50. <https://doi.org/10.1016/j.coastaleng.2017.10.012>